2024 IEEE International Conference on Robotics and Automation (ICRA 2024)
May 13-17, 2024. Yokohama, Japan

RoboBall: An All-Terrain Spherical Robot with a Pressurized Shell

Micah Oevermann, Derek Pravecek, Garrett Jibrail, Rishi Jangale, Robert O. Ambrose(*IEEE Member*)

***Abstract*— Spherical robots are a different type of mobility platform. A spherical robot is self-contained within its shell rather than relying on a chassis with wheels to navigate. In this shell, it is completely shielded from dust and the environment. This benefit of geometric simplicity has led to the spherical robot becoming an advantageous option for all-terrain exploration and surveying. This paper focuses on a novel iteration of such a robot with a pressurized pneumatic shell design. A soft robot of this type brings benefits of a passive, compliant contact surface that can affect its performance. However, the added softness of its shell adds new unmodeled dynamics into the system that impair commonly used control schemes. This paper outlines the design and manufacture of a soft, inflatable, spherical shell designed for a robot driven by an internal 2-DOF pendulum. In addition, it presents models for controlling the pendulum and understanding the shell dynamics. The paper concludes with experimental validations of these models and field tests of the system on slopes, gravel, rough grass, and on water.**

I. INTRODUCTION

NASA launched Artemis I in late 2022. The capsule and rocket launched as the start of a massive effort to return humans to the moon to explore the lunar south pole. One of the potential landing sites is on the lip of Shackleton crater, whose walls permanently shield its depths from sunlight. Deep and dark, these shadowed regions at the south pole harbor frozen water deposited over the eons. Exploration and utilization of Shackleton's depths will be paramount to the success of Artemis and future programs. However, the walls that shield sunlight also block radio contact with Earth, average 30°of downward slope, and are consistently at 40K or lower temperature. These are strong reasons to not send humans into its depths.

Autonomous and teleoperated robotic rovers replace the need for scientists to be physically present for exploration and surveying of dangerous and extreme environments. The first autonomous US wheeled rolling system to move on another planet was the Sojourner rover as part of the Mars Pathfinder missions. Sojourner used a passive rocker-bogie suspension system to allow it to maintain even ground pressure between its wheels. Its lack of dynamic springs and dampers limited its top speed but was sufficient for its designed velocity of <0.4KPH[1]. Another extraterrestrial mobility platform was the Lunar Roving Vehicle (LRV), driven by Apollo astronauts on the lunar surface with soft, mesh tires. The astronauts reported LRV performed exceptionally but had difficulties reaching higher speeds (>10 KPH) as a few or all of its wheels would occasionally come off the ground [2] most likely due to its suspension design in low gravity. The Chariot rover, built by NASA, addressed these issues by implementing an advanced redundant active suspension [3]. More recently, the VIPER rover is the next-generation lunar rover with active robotic suspension [4]. designed to descend into craters around the south pole while navigating soft soils. VIPER is limited to slopes of 15° and <6 hours of operation in the shadows. These famous examples show the significance of design, where understanding suspension dynamics and environmental exposure is vital to a lunar mission's success. Spherical robots offer an alternative to wheeled rover systems. State-of-the-art rovers, such as VIPER and Chariot, use a slow, methodical, and controlled approach to descend slopes and traverse terrain. Spheres, however, can take advantage of their natural locomotion mode of rolling and bouncing to descend a slope in a fast, semi-chaotic / semi-controlled motion. Its symmetric geometry ensures there is no orientation such that it could be trapped on its back, for it has no back. For this reason, it is ideal for rolling into inhospitable craters.

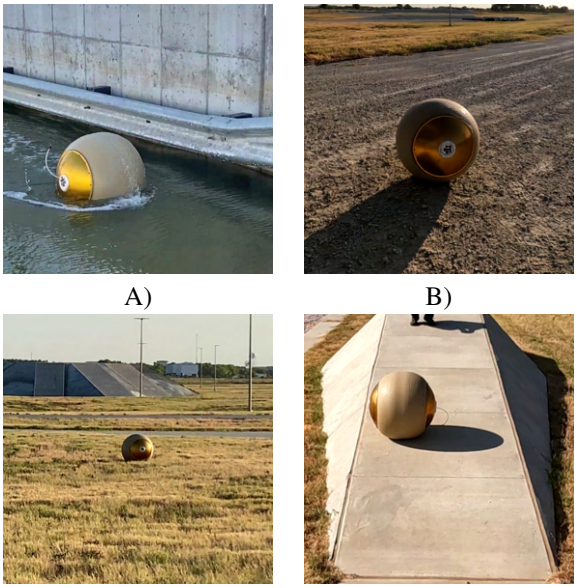

Fig. 1. RoboBall in various terrain: A) floating and maneuvering on water. The 1/4" pneumatic line in the left side is for pressurizing the system B) rolling over gravel C) rolling through grass) D) rolling down a 15% grade

Spherical robots consist of an interior driving mechanism and an outer shell. Popular driving mechanism designs use a combination of flywheels and pendula to achieve motion with a hard outer shell. Prototypes with two pendula [5] allow

**Research supported by the Texas A&M Chancellor's Research Initiative and matching funds from the Texas Governor's University Research Initiative.

Authors are with Texas A&M University, College Station TX, 77843 USA R.O Ambrose's e-mail is rambrose@tamu.edu

for sharp turns, added flywheels to enhance driving stability [6], or a combination of the flywheels and pendula [7]. Most make use of a hard outer shell and rely on complex control of their mechanisms or inertia flywheels to dampen disturbances and keep the system stable [8]. They overlook the benefits a soft outer shell could have on the system dynamics, possibly from the difficulty of manufacturing a soft spherical shell. A rolling sphere will naturally accelerate down a slope, so a soft outer layer would help dampen the dynamics of these types of systems, as well as help it tolerate uncertain terrain disturbances. This is similar to outfitting a car with pliable rubber tires, as opposed to rigid plastic ones.

There have been a few attempts at creating a spherical robot with a dynamically elastic shell. One attempt used a set of parallel elastic bars in the shell to allow for some impact absorption but did not state its impact on the robot dynamics [9]. Reference [10] iterates on the idea of flexible bars but relies on randomness for exploration, yielding an inefficient surveying system. Ylikorpi et al. investigated the effects of a pressurized pneumatic system on obstacle crossing [11]. The authors cite collision velocity as the main reason behind the system's ability to overcome obstacles but do not investigate the effect the system's internal pressure may have on its dynamics. The pressure of vehicle tires is an option for tuning system dynamics [12] and could apply for the spherical case as shown in [13]. This concept of pressure-based dynamics has yet to be thoroughly explored for motion control of spherical robots. Simply because very few systems employ a fully actuated inner mechanism with a fully pressurized and pneumatic shell.

In this paper, we present a novel design modification to existing spherical robots that improve their exploratory capabilities. The prototype spherical robot, dubbed RoboBall, is outfitted with a soft pressurized pneumatic outer shell driven by a 2-DOF robotic pendulum. The manufacturing process of this new shell is detailed. We show empirically that controllers derived under the assumption of a hard shell are sufficient, but controlled changes in the system's internal pressure influence performance. We present data showing the implementation of these controllers and how properties associated with pressure affect the system's dynamics and the robot's performance. These pressure-based dynamic properties have not been documented previously. Supplemental studies of the design's ruggedness are shown by rolling down slopes, across gravel, and over water are also presented in Figure 1.

II. Design of Inner Mechanism and Outer Shell

A. Robotic Pendulum Design

At a high level, the pendulum itself contains three main sub-assemblies: a driveshaft or "pipe", a pendulum, and a pitch module linking them shown in Figure 2. These three sections are constructed in series to form a 2-DOF pendulum with intersecting axis of rotation. By skewing the mass to the most radially distant sections of the pendulum, the center of gravity becomes eccentrically located, creating a rolling motion.

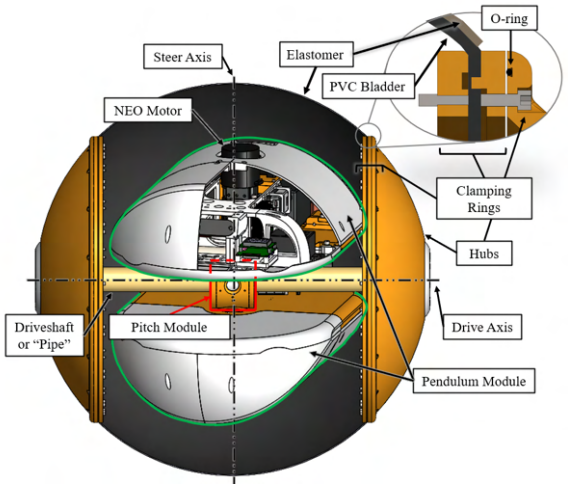

Fig. 2. Depiction of Pendulum Construction and Mounting Interface of Soft Shell

The basic electro-mechanical components are mainly sourced from a FIRST Robotics kit. Including Rev NEO BLDC motors (4 total: 2 on each axis) with built-in encoders, a RoboRio computer, and a Wi-Fi router for wireless communication with the host computer. Software and control algorithms were implemented in the WPILib software library for compatibility. Inputs to each axis are commanded from a PlayStation joystick connected to the host computer. Two VN-100 IMU sensors are rigidly attached to the pendulum and pitch module to measure system angles and shell pressure.

B. Novel Inflatable Shell Design

The outer shell is a two-layer polymer skin that serves as the interface between the robot and its environment. The inner layer is a plasticized PVC bladder (exercise ball or similar) which forms the airtight barrier between RoboBall and its surroundings. The outer layer is a military-grade spray-on elastomer [14] which constrains the inner layer from undesirable expansion at higher pressures. The elastomer bedliner forms the main traction surface of the system and protects the inner layer from punctures.

The construction and interfacing of the shell onto the robot introduce two additional components. The first is a series of large-diameter, anodized aluminum rings which clamp the bladder layer into a sealing groove, shown in Figure 2 close-up. These components allow the mounting of the deflated, flexible shell onto additional parts, called hubs. The hubs are large-diameter, anodized, aluminum domes that transmit the torque of the drivetrain to the shell, making mobility possible. The hubs also host a 1/4" pneumatic press in fitting for pressurization.

The process for constructing and assembling a shell is listed in the following section and illustrated in Figure 3.

1) Inflate a 60 cm (24 in.) plasticized PVC sphere, such as a yoga ball, into a rig that prevents rotation (Figure 3A).
2) Mark out circular regions to be cut out for the installation of the clamping rings.

3) Deflate and cut the ball along the markings.
4) Assemble inner and outer clamping rings to each side by drilling through the ball material with sealing fasteners (Figure 3B).
5) Inflate a second yoga ball inside the first (which can no longer be inflated) to recover its shape (Figure 3C).
6) Optional: Apply fiberglass tape to the bladder for extra reinforcement or to create tread patterns. (not illustrated)
7) Mask off the exposed surfaces of the clamping rings and apply 3mm (.125 in.) highly elastic spray-on elastomer (Figure 3D).
8) Allow the assembly to set for up to a full day (Figure 3E).
9) Attach the hubs onto the rings with sealing fasteners.
10) Pressurize the vessel to 3-5 psi to check for leaks (Figure 3F).

III. System Dynamic Model

To derive an initial model, we assume that the outer shell does not deform significantly and is a circle. Additionally, we assume that the robot can be modeled as a planar system in a hoop with a 1-DOF pendulum, then twisted 90° about the vertical to represent the other axis. The system states are shown in Figure 4, where ϕ is the absolute tilt angle of the driveshaft with respect to the ground, θ_g is the angle the pendulum makes with the ground, and θ is the relative angle between the pendulum and the shaft. This relative angle is measured by an encoder and actuated with a motor, τ_m. Both ϕ and θ_g are measured by IMUs rigidly attached to the frame. The angles of ϕ, θ, and θ_g are related through Equation (1).

$$\theta_g = \phi + \theta \tag{1}$$

Similarly, R is the nominal outer radius of the ball without deformation and r is the distance to the center of gravity of the pendulum from the axis of rotation. d_{flat} is the diameter of the flat section of the shell resting on the ground and is assumed to be zero initially.

We can then define the system energy with respect to absolute angles: ϕ and θ_g. Potential and kinetic energies are shown in Equations (2) – (4).

$$V = m_p g\left(R - r\cos(\theta_g)\right) \tag{2}$$

$$T_{rot} = \frac{1}{2} I_b \dot{\phi}^2 + \frac{1}{2} I_p \dot{\theta}_g^2 \tag{3}$$

$$T_{trans} = \frac{1}{2} m_b (R\dot{\phi})^2 + \frac{1}{2} m_p (\dot{x}_p^2 + \dot{y}_p^2) \tag{4}$$

Where m_p, m_b, I_p, and I_b are the masses and rotational inertias of the pendulum and ball shell respectively. The pendulum translational energies can be expressed with $x_p = R\phi - r\sin(\theta_g)$ and $y_p = (R - r\cos(\theta_g)$. To find the planar equations of motion we use Lagrange's method for $L = T_{rot} + T_{trans} - V$.

$$\frac{\partial}{\partial t}\frac{\partial L}{\partial \dot{q}} - \frac{\partial L}{\partial q} = \tau_q \tag{5}$$

Applying equation (5) with $q = \phi$ and θ_g yields the following EOMs:

$$\tau_m = I_{eq}\ddot{\phi} - m_p r R\cos(\theta_g)\ddot{\theta}_g + m_p r R\sin(\theta_g)\dot{\theta}_g^2 \tag{6}$$

$$-\tau_m = -m_p r R\cos(\theta_g)\ddot{\phi} + (I_p + m_p r^2)\ddot{\theta}_g + m_p r g\sin(\theta_g) \tag{7}$$

where $I_{eq} = (m_b + m_p)R^2 + I_b$

which can be simplified to the standard robotic form

$$M(\theta_g)\begin{pmatrix}\ddot{\phi}\\ \ddot{\theta}_g\end{pmatrix} + C(\dot{\theta}_g, \theta_g)\begin{pmatrix}\dot{\phi}\\ \dot{\theta}_g\end{pmatrix} + V(\theta_g) = F\tau_m \tag{8}$$

where

$$M(\theta_g) = \begin{bmatrix} I_{eq} & -m_p r R\cos(\theta_g) \\ -m_p r R\cos(\theta_g) & I_p + m_p r^2 \end{bmatrix}$$

$$C(\dot{\theta}_g, \theta_g) = \begin{bmatrix} 0 & m_p r R\sin(\theta_g)\dot{\theta}_g \\ 0 & 0 \end{bmatrix}$$

$$V(\theta_g) = \begin{bmatrix} 0 \\ m_p r g\sin(\theta_g) \end{bmatrix} \quad F = \begin{bmatrix} 1 \\ -1 \end{bmatrix}$$

IV. Model of the Soft Shell

A rigid sphere will contact a flat surface at exactly one point. However, inflatable bodies deform to the surface that they rest on. This deformation is also dependent on pressure as objects at higher pressure will deform less. For RoboBall, this deformed patch or "flat" will be our primary traction surface, and has the greatest effect on the system dynamics. We propose a model for the flat in this section. A sketch of the deformed surface is shown in Figure 5. Where δ represents how much the ball has deformed from a perfect sphere, W_b is the total weight of the system, and P is internal system pressure.

We can relate R, δ, and d_{flat} through the Pythagorean Theorem shown in Equation (9). A constraint must be placed on δ such that the compressed shell does not interfere with the pendulum. For our system that was to keep a pressure such that $\delta < 2$ in.

$$R^2 = (\frac{1}{2}d_{flat})^2 + (R - \delta)^2 \tag{9}$$

The flat that supports the weight of the system through pneumatic pressure, P, over the flat area, must equal the weight of the system to be in equilibrium. Given in Equation (10).

$$\sum F = W_{ball} = A_{flat}P = P\frac{\pi}{4}d_{flat}^2 \tag{10}$$

Rearranging Equation (10) to Equation (11) yields a model relating the flat to system pressure which is plotted in Figure 7. Where $W_b = (m_b + m_p)g$ from Table I.

$$d_{flat} = \sqrt{\frac{4W_b}{\pi * P}} \tag{11}$$

A. Validation of Soft Shell Model

To verify Equation (11), the robot was placed on a clear polycarbonate table with a tape measure beneath it. A light was shown to add contrast to the deformed and undeformed regions. The robot was then manually inflated to a pressure and the diameter of the flat was recorded. A picture of the test setup is shown in Figure 6. The results were then plotted against the model, this is shown in Figure 7. The data fits in the middle but becomes a poor fit on the extremes. For low pressures, the stiffness of the polymer adds more structure

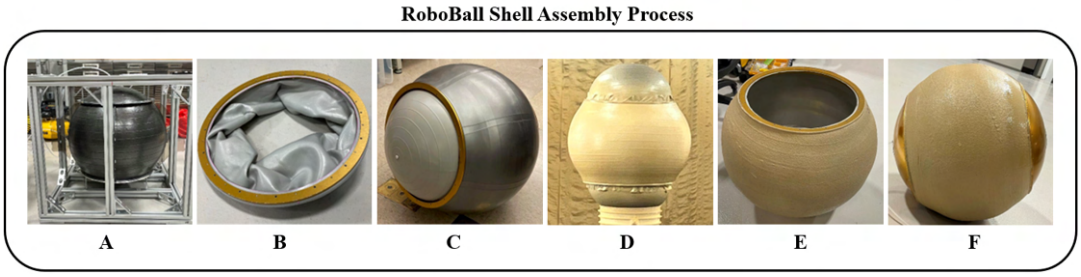

Fig. 3. Illustration of RoboBall "Soft Shell" Manufacturing Process

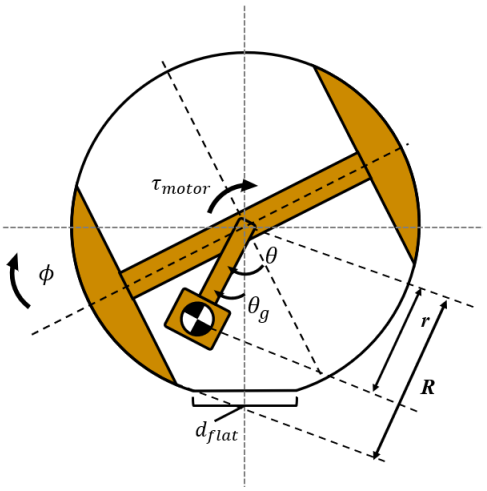

Fig. 4. Schematic of Robot States

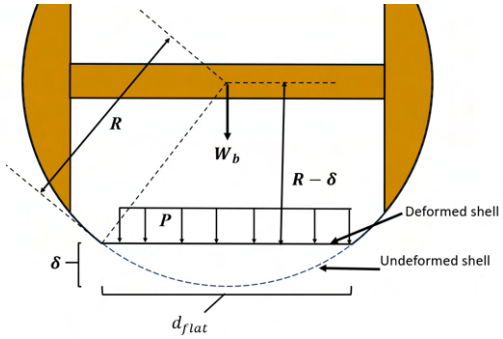

Fig. 5. Schematic Relating Geometry of a Flat of Pressurized System (rolling out of page)

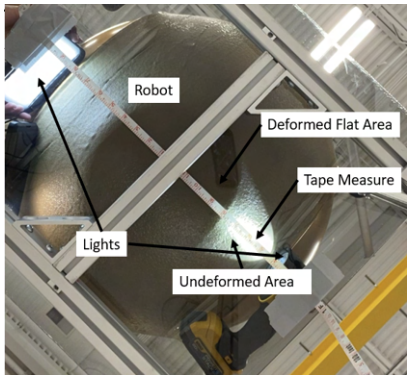

Fig. 6. Measurement of the Flat from below

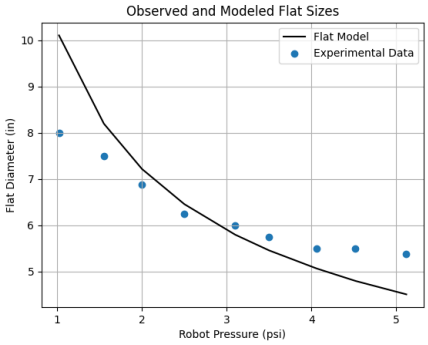

Fig. 7. Comparison of Flat Model with Experimental Data

and prevents the flat from growing. At higher pressures, the change in diameter is less pronounced and the shell stiffness would also work against a change in shape.

V. Controller Design

In this section, we will derive and validate two different controllers for the steering (lateral) and driving (longitudinal) motions of the system. These methods use the same EOMs, but the control goal differs. For steering, the driveshaft or "pipe" angle, ϕ, is held at a point to achieve a direction. For driving, the outer shell speed, $\dot{\phi}$, is controlled to give the robot a velocity.

A. Linear Quadratic Control of Steering

In Equation (8) the matrix F has a rank less than two, meaning this system is under-actuated. Linear Quadratic Regulators (LQRs) have been a popular choice for regulating similar systems in previous works [15], so we present a similar derivation here. We can simplify (6) and (7) by assuming low speeds and small angles such that $\dot{\theta}_g^2 \approx 0$, $\sin(\theta_g) \approx \theta_g$ and $\cos(\theta_g) \approx 1$. These simplified equations become (12) and (13).

$$\tau = I_{eq}\ddot{\phi} - m_p r R \ddot{\theta}_g \tag{12}$$

$$-\tau = -m_p r R \ddot{\phi} + (I_p + m_p r^2)\ddot{\theta}_g + m_p r g \theta_g \tag{13}$$

these equations can be manipulated into the form of (14) where $x = (\phi, \theta_g, \dot{\phi}, \dot{\theta}_g)$.

$$\dot{x} = Ax + B\tau \tag{14}$$

By substituting values from Table I, (14) yields the following A and B matrices:

$$A = \begin{bmatrix} 0 & 0 & 1 & 0 \\ 0 & 0 & 0 & 1 \\ 0 & -6.22 & 0 & 0 \\ 0 & -40.2 & 0 & 0 \end{bmatrix} \quad B = \begin{bmatrix} 0 \\ 0 \\ 0.0128 \\ 1.57 \end{bmatrix} \tag{15}$$

Solving the optimal control problem requires minimizing a cost function (16) according to chosen weighted matrices Q and R.

$$J = \int \left(x^T Q x + \tau_m^T R \tau_m\right) dt \tag{16}$$

We refined the values of Q and R based on experiments with the robot in its shell to achieve acceptable performance and stability.

$$Q = \begin{bmatrix} 1000 & 0 & 0 & 0 \\ 0 & 1 & 0 & 0 \\ 0 & 0 & 10 & 0 \\ 0 & 0 & 0 & 1 \end{bmatrix} \quad R = \begin{bmatrix} 5 \end{bmatrix} \tag{17}$$

These matrices can then be used to solve the optimal Linear Quadratic Regulator [16, Ch. 9] problem to yield a linear feedback control law (18) which stabilizes the linear system (12) and (13).

$$\tau_m = -Kx \tag{18}$$

For our system, the K matrix was obtained offline and loaded into the robot on startup. All states are available for measurement from encoders and onboard IMUs.

B. Model-Based P Control of Drive Direction

We derive a controller for the drive direction to by assuming the reaction torque in (6) and (7) are positive. Then solving (7) for $\ddot{\theta}_g$ and substituting into (6) to yield (19)

$$\begin{aligned} \tau_m = \frac{1}{\gamma}((I_{eq}(I_p + m_p r^2) + (m_p r R \cos(\theta_g))^2)\ddot{\phi} \\ +(I_p + m_p r^2) m_p r R \sin(\theta_g)\dot{\theta}_g^2 \\ +(m_p r)^2 R g \cos(\theta_g)\sin(\theta_g)) \end{aligned} \tag{19}$$

Substituting $\ddot{\phi}$ with (20) allows the robot to track velocity.

$$\ddot{\phi} = K_p(\dot{\phi}_{desired} - \dot{\phi}) \tag{20}$$

VI. Experimental Validation of Controllers

Both controllers use parameters measured from a CAD model of the robot and shown in Table I.

A. Validation of Steering Controller

To validate that the linear controller would stabilize the full nonlinear, system we integrated equations (6), (7), and (18) with a non-zero driveshaft angle, ϕ. This is similar to setting the robot on its side and letting it balance itself. The integration results are shown in Figure 8. The results show that the linear feedback will re-balance the system for large angles. These equations and controller were derived under

TABLE I
Parameter Values

Symbol	Description	Value [units]
m_p	mass of the pendulum	22.65 $[kg]$
m_b	mass of the ball or shell	14.49 $[kg]$
I_p	the inertia of the pendulum	0.4279 $[kgm^2]$
I_b	the inertia of the shell	0.902 $[kgm^2]$
R	outer radius of shell	0.305 $[m]$
r	radius to c.g. pf pendulum	0.0975 $[m]$
g	gravitational constant	9.81 $[m/s^2]$
τ_m	input motor torque	$[Nm]$

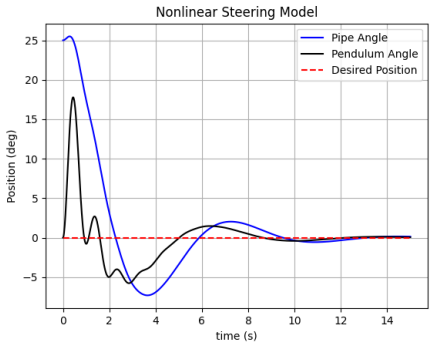

Fig. 8. LQR Feedback Simulated on Full Nonlinear System

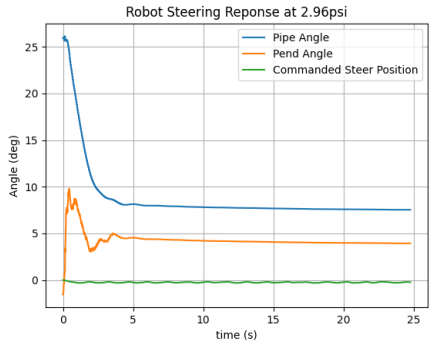

Fig. 9. Experimental Results of LQR Feedback on Experimental Robot with a Soft Shell inflated to 2.96psi

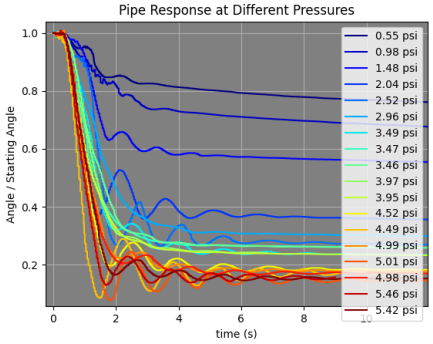

Fig. 10. LQR Stabilization of the System at Different Pressures

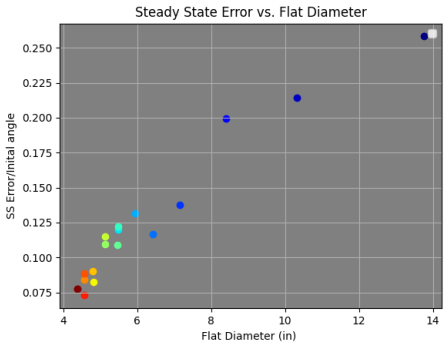

Fig. 11. Steady State Steering Error Plotted against Flat Diameter Model

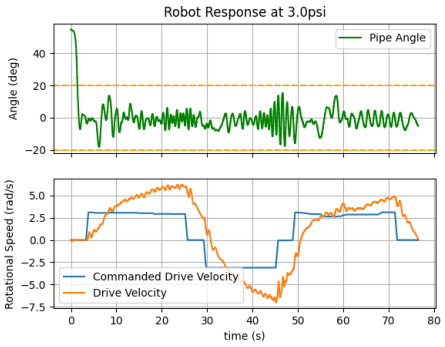

Fig. 12. Experimental Validation of the Driving Controller

the assumption of a circular shell, which is the reason that all states track to zero in this ideal case.

The results of running the controller on RoboBall, pressurized to 3psi, while not driving, are shown in Figure 9. The system exhibits a more critically damped response and significant steady-state error. This indicates that the shell stiffness, damping, and flat size could be affecting its performance. Since these are not considered in the controller derivation.

To further investigate the effect pressure has on the system, the same balancing experiment was conducted at different system pressures from 0.5 to 5.5 psi. The compiled results are shown in Figure 10. To simplify comparison, the data is normalized with respect to its initial position. Low pressures are colored blue while higher pressures are red to show the spectrum of responses. As the pressure increases, both the steady state error, and flat diameter (Figure 7) decrease.

To establish a correlation, the steady-state error from Figure 10 was plotted against the model for the flat sizes, equation (11), evaluated at the measured shell pressure. This is shown in Figure 11 with colors representing increasing pressure. The obvious positive correlation between the steady state error and the flat size points to its effects on the steering controller's performance.

B. Empirical Testing of Full System

The results of the robot tracking an input velocity at 3.0psi is shown in Figure 12. RoboBall is commanded to drive forward, reverse, and drive forward again on flat concrete. While the robot attempts to balance itself, as shown in the pipe angle plot. The pipe angle is bounded within about 20°. Recall that the flat diameter is 3 psi is about 6in, or about a 29°arc for a 12in radius ball. Additionally, from Figure 9 at 2.96psi there was a steady state balancing error of around 7.5°, or 14°total for both directions. This indicates potential a "dead-zone" between 14°and 29°in size where the steering controller is unable to accurately balance the robot while driving. This deficiency in control authority leads to a wobbling behavior that can cause the system to go unstable at higher speeds.

C. Supplemental Terrain and Ruggedness Testing

Although the pressure of the system does significantly affect its accuracy, the control scheme is still sufficient for basic maneuvering of the system in various terrains shown in Figure 1. The system performs extremely well in water since the floating system has no flat (Figure 1A). As well as other types of terrain such as gravel or rough grass (Figure 1B-C) but had trouble reaching high speeds due to external disturbances caused by the terrain, and the "dead zone" previously described. Figure 1D shows the system performing a controlled descent down a 15% slope as an analogy to rolling into a crater. A video of these experiments and summarizing some other aspects of this paper is shown in [17].

D. Conclusion and Future Work

This paper describes the value suspension design has on a rover's success. Noting that most spherical robots are implemented with hard outer shells. By changing the design of an outer shell from a hard to a soft variety we could get similar advantages as rubber tires to a car. With this rationale, we present an implementation of a spherical robot with a soft outer shell to act as a suspension. However, by equipping the robot with this new soft shell we identified new pressure-based dynamic problems associated with this type of system that affect popular control methods. Despite these issues, the robot and shell are still rugged and stable enough for basic maneuvers outside of a lab.

Future work will focus on improvements to the shell modeling and control scheme. Iterations on the soft shell model will be made to better account for discrepancies in the upper and lower pressure regions. A more accurate model will allow for better prediction of the contact patch area and the contact dynamics. Additionally, including the observed dynamics in the feedback control scheme will help with improving the steady-state balancing error and improve performance.

REFERENCES

[1] *Rover Wheels*. https://mars.nasa.gov/mer/mission/rover/wheels-and-legs/.. Accessed: 29 August 2023.

[2] *"Apollo 16 Mission Report", MSC-07230*. Tech. rep.

[3] Bill Bluethmann et al. "An active suspension system for lunar crew mobility". In: *2010 IEEE Aerospace Conference*. 2010, pp. 1–9. DOI: 10.1109/AERO.2010.5446895.

[4] Cyndia Cao, Arno Rogg, and Antoine Tardy. "Actuated Suspension Tuning Characterization of the VIPER Lunar Rover". In: *2023 IEEE Aerospace Conference*. 2023, pp. 1–11. DOI: 10.1109/AERO55745.2023.10115796.

[5] Sung-Su Ahn and Yun-Jung Lee. "Novel Spherical Robot with Hybrid Pendulum Driving Mechanism". In: *Advances in Mechanical Engineering* 6 (2014), p. 456727. DOI: 10.1155/2014/456727.

[6] Han Mao et al. "A Spherical Mobile Robot Driven by Eccentric Pendulum and Self-stabilizing by Flywheel". In: *2020 17th International Conference on Ubiquitous Robots (UR)*. 2020, pp. 169–174. DOI: 10.1109/UR49135.2020.9144903.

[7] Muhammad Affan Arif et al. "Design of an Amphibious Spherical Robot Driven by Twin Eccentric Pendulums With Flywheel-Based Inertial Stabilization". In: *IEEE/ASME Transactions on Mechatronics* (2023), pp. 1–13. DOI: 10.1109/TMECH.2023.3247641.

[8] Yixu Wang et al. "Robust servo linear quadratic regulator controller based on state compensation and velocity feedforward of the spherical robot: Theory and experimental verification". In: *International Journal of Advanced Robotic Systems* 20.2 (2023), p. 17298806231153229. DOI: 10.1177/17298806231153229.

[9] Jayoung Kim, Hyokjo Kwon, and Jihong Lee. "A rolling robot: Design and implementation". In: *2009 7th Asian Control Conference*. 2009, pp. 1474–1479.

[10] S. Mintchev et al. "A Soft Robot for Random Exploration of Terrestrial Environments". In: *2018 IEEE International Conference on Robotics and Automation (ICRA)*. 2018, pp. 7492–7497. DOI: 10.1109/ICRA.2018.8460667.

[11] Tomi J. Ylikorpi, Aarne J. Halme, and Pekka J. Forsman. "Dynamic modeling and obstacle-crossing capability of flexible pendulum-driven ball-shaped robots". In: *Robotics and Autonomous Systems* 87 (2017), pp. 269–280. ISSN: 0921-8890. DOI: https://doi.org/10.1016/j.robot.2016.10.019. URL: https://www.sciencedirect.com/science/article/pii/S0921889015302530.

[12] B.T. Adams et al. "Effects of central tire inflation systems on ride quality of agricultural vehicles". In: *Journal of Terramechanics* 41.4 (2004), pp. 199–207. ISSN: 0022-4898. DOI: https://doi.org/10.1016/j.jterra.2004.02.011. URL: https://www.sciencedirect.com/science/article/pii/S0022489804000382.

[13] Meghali Prashant Dravid. "Design and Modeling of a Soft, Pressurised, Spherical Robot". Texas AM University, 2022.

[14] *BattleJacket® CRS TDS Data Sheet*. Rev. 1. Rhino Linings USA. URL: https://rhinolinings.com/tech-center/.

[15] Russ Tedrake. *Underactuated Robotics. Algorithms for Walking, Running, Swimming, Flying, and Manipulation*. 2023. URL: https://underactuated.csail.mit.edu.

[16] Bernard Friedland. *Control System Design: An Introduction to State Space Methods*. Dover Publications, 1985.

[17] *RoboBall Experiments. https://youtu.be/doiLKlk2Rl8*.